Vietnam Journal of Earth Sciences, 47(3), 376–395, https://doi.org/10.15625/2615-9783/23301

Vietnam Journal of Earth Sciences
https://vjs.ac.vn/index.php/jse

Metamorphism in the A Vuong Formation, southern Truong Son Belt, Vietnam

Vuong Bui Thi Sinh[1,2*], Ippei Kitano[2], Tuan-Anh Tran[1], Can Pham-Ngoc[1], Ly Vu Hoang[1], Lien Pham Thi Phuong[1], Thi Huong Ngo[1], Cong Tran Quoc[1]

[1]*Institute of Earth Sciences, Vietnam Academy of Science and Technology, Hanoi, Vietnam*
[2]*The Hokkaido University Museum, Hokkaido University, Hokkaido 060-0810, Japan*

Received 02 May 2025; Received in revised form 06 July 2025; Accepted 13 August 2025

ABSTRACT

The A Vuong Formation, located within the southern Truong Son Belt in central Vietnam, comprises low- to high-grade metamorphic rocks that record crucial insights into the region's tectonic evolution. Our field investigations reveal that it mainly consists of the psammitic and pelitic schists, intercalated with some mafic or siliceous layers, and locally cut by leucocratic veins. The indicative mineral assemblages in the pelitic to psammitic schists define two metamorphic zones: a greenschist-facies biotite-chlorite zone and an amphibolite-facies staurolite zone. Based on conventional geothermobarometry, the peak metamorphic condition in the staurolite zone was estimated at *ca.* 5.5–8.7 kbar and 590–640°C, followed by a retrograde stage at 4.4–7.4 kbar and 530–570°C. Notably, a porphyroblastic andalusite observed in a pelitic schist from this zone is rimmed by kyanite with a preferred orientation. In addition, it includes kyanite, sillimanite, and an intergrowth of staurolite + quartz as inclusions. These features suggest their equilibrium during the prograde stage, reflecting a pressure-temperature transition from andalusite to kyanite stability. The prograde metamorphic condition is thus constrained at the triple point of andalusite-kyanite-sillimanite. The petrological evidence and estimated metamorphic conditions for the current pelitic schists support a unique anti-clockwise pressure-temperature trajectory, rather than a clockwise one. Its thermobaric feature is well aligned with the amphibolite-facies metamorphism of the neighboring Dai Loc Complex, and contrasts with that of the Kham Duc Complex (Kontum Massif).

Keywords: A Vuong Formation, Truong Son Belt, Anti-clockwise *P-T* trajectory, Biotite-Chlorite zone, Staurolite zone.

1. Introduction

The Truong Son Belt (TSB), a part of the Trans Vietnam Orogenic Belt (Osanai et al., 2008) in the eastern Indochina Block, has experienced multiple tectono-thermal events (Fig. 1a). At its southern end, the Dai Loc Complex (DLC) records extensive early Paleozoic magmatic activities (e.g., Carter et al., 2001; Pham et al., 2016; Jiang et al., 2020; Nguyen et al., 2021) along with minor occurrences of granulite-facies metamorphic rocks (Bui et al., 2022, 2023; Kitano et al., 2022; Nguyen et al., 2023). Recent studies have paid attention to these high-grade metamorphic rocks in the late Ordovician to early Devonian Dai Loc granitic complex, due

*Corresponding author, Email: buisinhvuongdc@gmail.com

to their crucial role in constraining the tectonic evolution of the TSB during the early Paleozoic. However, conflicting bimodal ideas have emerged regarding the nature of metamorphic history (Bui et al., 2022; Nguyen et al., 2023). As a consensus, the Dai Loc pelitic gneisses underwent sillimanite-stable granulite-facies metamorphism, associated with voluminous granitic magmatism at *ca.* 430–450 Ma, followed by a kyanite-stable amphibolite-facies metamorphic stage and mylonitization (Bui et al., 2022; Nguyen et al., 2023). On the one hand, the later amphibolite-facies stage has been considered retrograde metamorphism, resulting from post-peak, subsequent isobaric cooling during the early Devonian (Bui et al., 2022, 2023). On the other hand, Nguyen et al. (2023) argued that it represents a distinct Triassic event during the Indosinian orogeny. To resolve this debate over the metamorphic process of pelitic gneisses in the DLC, a new approach is necessary.

This study focuses on the A Vuong Formation (AVF), which surrounds the DLC (Figs. 1b-c). The formation is a weakly metamorphosed sedimentary sequence, accompanied by traces of contact metamorphism related to local Dai Loc granitoid intrusions (Thuc et al., 1995; Tran and Vu, 2011), and the occurrence of kyanite-bearing schists (Nguyen et al., 2023). These geological features suggest a possible tectonic relationship between the AVF and the DLC, involving both granitic magmatism and kyanite-stable metamorphism. Thus, the metamorphic evolution of the AVF has the potential to be linked with the kyanite-stable amphibolite-facies metamorphic stage, observed in the pelitic gneisses of the DLC, and shed new light on their tectonics. However, the lack of systematic geological and petrological analyses in the AVF has left its metamorphic framework poorly understood. This further hinders efforts to reconstruct the early Paleozoic tectono-thermal evolution of the southern TSB.

The present study conducted preliminary geological and petrographical investigations of the AVF, then defined the progressive metamorphism and metamorphic conditions of the rocks based on conventional thermobarometry. These findings were then compared with those of the DLC to better understand the nature of metamorphism in the AVF and its local tectonic linkage with the DLC. The mineral abbreviations used in this study follow Whitney and Evans (2010).

2. Geological outline

The Sibumasu, Indochina, and South China Blocks are three major cratonic blocks of Southeast Asia (Fig. 1a). The collision between the Indochina and South China Blocks during Permian-Triassic resulted in the formation of the Trans Vietnam Orogenic Belt (Osanai et al., 2008), which induced high-grade metamorphism, intense deformation and magmatism in the Indochina Block. These effects are especially evident along the major tectonic features such as the Red River shear zone, the Song Ma suture zone, the Tam Ky-Phuoc Son (TKPS) shear zone, and the Dak To Kan shear zone (Fig. 1a). Furthermore, over the last two decades, extensive early Paleozoic magmatism and high-grade metamorphism have also been identified in the southern part of the Indochina Block (Usuki et al., 2009; Nakano et al., 2013; Pham et al., 2016; Nguyen et al., 2019; and references therein), especially in the Kontum Massif (KTM) and the TSB. These geological units are separated by the TKPS shear zone (Fig. 1a).

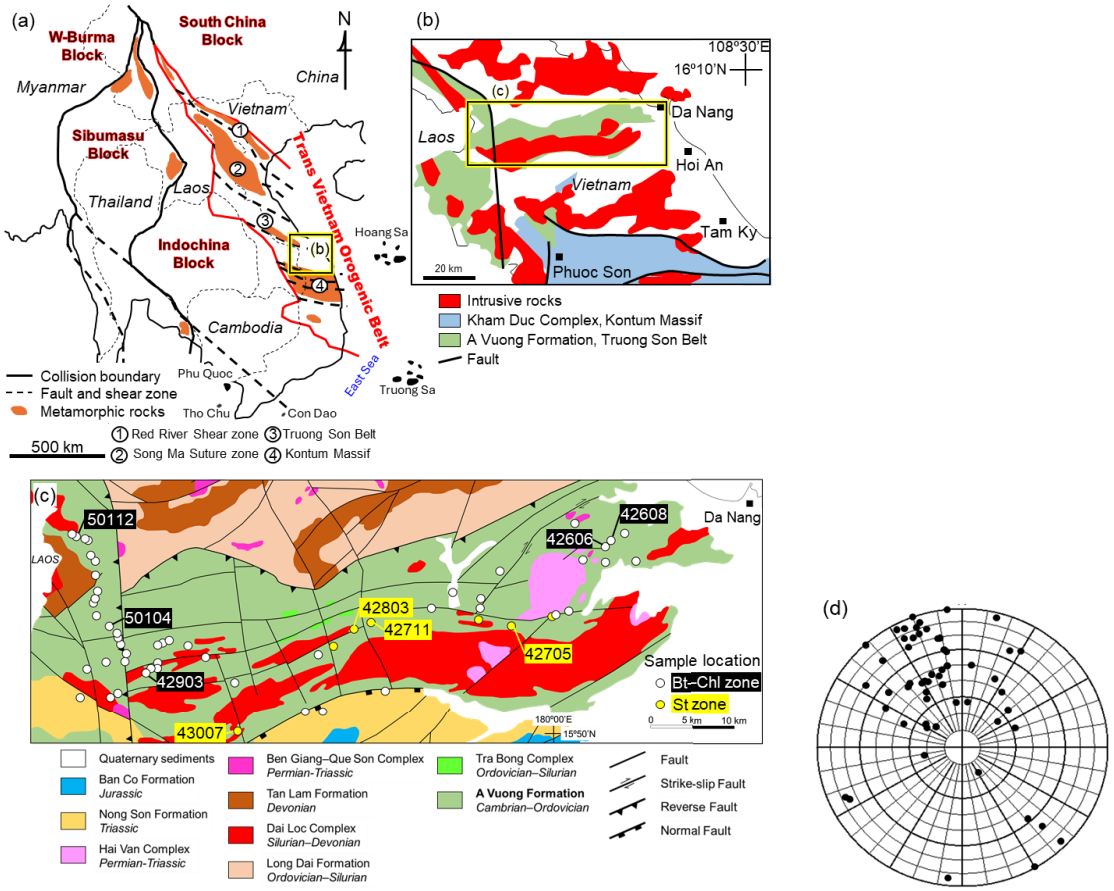

Figure 1. (a) Tectonic map of the Trans Vietnam Orogenic Belt between the South China Block and Indochina Block in Southeast Asia (after Osanai et al., 2008). (b) Simplified geological map for A Vuong Formation in the Truong Son Belt, Kham Duc Complex in the Kontum Massif, and intrusive rocks after Nguyen (1995, 1996a, 1996b). (c) Geological map of the study area modified after Nguyen (1995, 1996a, 1996b) and Tran and Vu (2011). The sample locations are shown with white circles for the biotite-chlorite zone and yellow circles for the staurolite zone, with some location numbers. (d) Schmidt diagrams (lower hemisphere) showing poles to foliation planes of phyllites and schists in the A Vuong Formation with black circles. NE-SW strike with southward dipping is dominant

The KTM is considered the core of the Indochina Block and is known to have undergone two distinct thermal events during the Ordovician-Silurian (e.g., Nagy et al., 2001; Usuki et al., 2009; Nakano et al., 2013; Ngo et al., 2025) and Permian-Triassic periods (e.g., Lepvrier et al., 1997, 2004; Osanai et al., 2004, 2008; Nakano et al., 2007, 2009, 2013; Bui et al., 2020). This massif consists of three plutono-metamorphic complexes: the Kannack Complex in the south, Ngoc Linh Complex in the center, and Kham Duc Complex in the north. These complexes experienced similar clockwise metamorphic pressure (*P*)-temperature (*T*) paths during the Permian-Triassic (e.g., Nakano et al., 2004, 2007, 2009; Osanai et al., 2004; Usuki et al., 2009). While the Ngoc Linh and Kannack Complexes consist mainly of high-*P* to ultrahigh-*P*, high-*T* to ultrahigh-*T* granulite-facies metamorphic rocks and minor amphibolite-facies ones (Nakano et al., 2004, 2007; Osanai et al., 2004; Faure et al., 2018), the Kham Duc Complex comprises metapelite,

metapsammite, and paragneiss ranging from greenschist- to amphibolite-facies (e.g., Nakano et al., 2009, 2013).

The TSB is a NW-SE trending, long tectonic belt across Vietnam and Laos within the Indochina Block, characterized by numerous faults and suture zones (e.g., Sanematsu et al., 2011). It is bounded by the Song Ma suture zone in the north and the TKPS shear zone in the south (Lepvrier et al., 2004; Tran et al., 2014; Shi et al., 2015; Nguyen et al., 2019) (Fig. 1a). The TSB predominantly contains Paleozoic to Mesozoic volcanic-sedimentary intruded by numerous plutonic rocks of various ages (Tran and Vu, 2011), along with minor metamorphosed rocks (Carter et al., 2001; Lepvrier et al., 2004; Sanematsu et al., 2011; Tran and Vu, 2011; Shi et al., 2015; Pham et al., 2016; Faure et al., 2018; Thassanapak et al., 2018; Jiang et al., 2020; Nguyen et al., 2021). Extensive Paleozoic-early Mesozoic magmatism during the Permian-Triassic (Tran et al., 2005, 2008; Luong et al., 2024) and Ordovician-Silurian (Shi et al., 2015; Gardner et al., 2017; Wang et al., 2020), with minor Cambrian (Shang and Chen, 2022; Ngo et al., 2024), has been identified in this belt. Greenschist- to amphibolite-facies metamorphic rocks occur sporadically along the faults or suture zones (Lepvrier et al., 2004; Nakano et al., 2013). In the southern part of the TSB, adjacent to the TKPS shear zone, early Paleozoic rocks, including the DLC and AVF (Figs. 1b-c), are dominant. The DLC features significant exposures covering several hundred square kilometers (Thuc et al., 1995), with primary lithologies of biotite-bearing granodioritic gneiss, muscovite granitic gneiss, mylonitic granitoids, and some aplitic dykes (e.g., Pham et al., 2016). It intrudes into the Cambrian-Ordovician AVF and is partly overlain by Cenozoic sediments to the east (Thuc et al., 1995; Wang et al., 2020). A part of the Dai Loc granitoid is covered by basal conglomerate of the early Devonian Tan Lam Formation (Tran and Vu, 2011). Additionally, recent studies have reported the granulite-facies metamorphic rocks in the DLC (Bui et al., 2022; Kitano et al., 2022; Nguyen et al., 2023).

The AVF lies unconformably on the Kham Duc and Nui Vu Complexes and is itself unconformably covered by the Long Dai Formation (Tran et al., 2020). The Nui Vu Complex is dominantly distributed in the northern part of the Kham Duc Complex. It consists of meta-extrusive rocks (mafic to felsic components) intercalated within metasandstones and metapelites (Nguyen et al., 2019). The AVF comprises Cambrian to lower Ordovician volcano-sedimentary rocks, which were weakly metamorphosed (quartz-sericite schist, quartzite, carbonaceous schist, and marble), interleaved with meta-mafic rocks (Hung, 1996; Tran et al., 2020; and references therein). The overlying Long Dai Formation is characterized by a basal conglomeratic unit and a coarse-grained graywacke sandstone unit, followed by an upper sequence of Ordovician-lower Silurian siltstone, sandstone, black shale, striped cherty shale, clay-chlorite shale, and gritstone (e.g., Nguyen, 1996a, b; Tran and Vu, 2011). The AVF is locally intruded by Dai Loc granitoids and Permian-Triassic intrusion of the Hai Van Complex and Ben Giang-Que Son Complex, causing localized contact metamorphism (Thuc et al., 1995; Nguyen, 1995, 1996a, b; Tran and Vu, 2011; Pham et al., 2021; Nguyen et al., 2024). The ubiquitous occurrences of kyanite-bearing schists were recently reported by Nguyen et al. (2023). Detrital U-Pb zircon dating provides a maximum depositional age of 516 Ma for the AVF (Wang et al., 2016).

3. Analytical methods

All analyses were conducted at Hokkaido University. Representative low- to high-grade metamorphic rocks from the study area were selected for the petrographic description. The aluminosilicate phases were identified by Raman spectroscopy (HORIBA XploRA PLUS system). Mineral chemistry was

obtained from a high-grade schist sample (42803B), which contains a suitable mineral assemblage for conventional geothermobarometry calculation of *P-T* estimates. The corresponding thin section was carefully polished with diamond paste in advance to ensure analytical accuracy. Backscattered electron images were acquired using a scanning electron microscope equipped with an energy dispersive X-ray spectroscopy (JEOL JSM-IT200). Quantitative analyses were performed by using a JEOL JXA-8800R electron probe microanalyzer with an accelerating voltage of 15 kV, a beam current of 10 nA, and a beam diameter of 2 μm. Data processing was carried out with a ZAF correction program. Natural minerals and synthetic metals were used as calibration standards. Representative mineral chemistry results are presented in Table 1. X-ray elemental mapping of garnet (Mg, Mn, Fe, and Ca) was performed using a beam current of 150 nA and a beam diameter of 5 μm.

Table 1. Representative chemical compositions of major minerals

	Medium-grained Grt	**Fine-grained Grt**	**Bt with fine-St**	**Bt with Ms**	**Bt with Ky & St**	**Ms with Bt**	**Ms with St**	**Ms with Ky**	**St in Grt rim**	**Fine-grained St**	**Medium-grained St**	**St + Qz**	**Pl near Grt**	**Pl near Bt**
No.	1-3	1-65	1-21	1-55	1-78	1-57	1-47	1-74	1-1’	1-19	1-45	1-71	1-41	1-31
SiO_2	38.01	38.22	36.04	36.23	36.71	46.20	46.54	46.17	29.37	28.79	29.12	27.46	67.11	66.34
TiO_2	0.06	0.05	2.49	2.37	2.01	0.56	0.42	0.40	0.83	0.74	0.61	0.45	0.03	0.00
Al_2O_3	21.12	20.75	19.13	19.35	20.21	34.93	35.32	35.97	53.32	53.60	53.84	54.09	21.55	21.56
Cr_2O_3	0.07	0.05	0.03	0.12	0.03	0.04	0.08	0.00	0.10	0.02	0.02	0.06	0.02	0.00
FeO	31.71	31.49	18.27	18.69	17.72	0.95	0.89	0.84	12.26	12.21	12.08	12.01	0.21	0.14
MnO	6.97	7.73	0.16	0.21	0.13	0.00	0.06	0.00	0.46	0.41	0.51	0.45	0.05	0.00
MgO	2.98	2.67	9.77	9.40	9.49	0.41	0.42	0.50	1.69	1.50	1.34	1.32	0.01	0.02
ZnO									0.32	0.55	0.58	0.55		
CaO	0.63	0.51	0.01	0.00	0.00	0.00	0.02	0.01	0.00	0.00	0.00	0.00	2.18	1.61
Na_2O	0.04	0.01	0.27	0.30	0.43	1.37	1.24	1.21	0.02	0.00	0.08	0.04	10.87	10.40
K_2O	0.04	0.01	8.72	8.84	8.82	9.64	9.58	9.76	0.01	0.01	0.01	0.00	0.09	0.69
Total	**101.61**	**101.47**	**94.87**	**95.51**	**95.56**	**94.09**	**94.56**	**94.84**	**98.38**	**97.83**	**98.18**	**96.43**	**102.11**	**100.76**
Oxygen No.	12	12	22	22	22	22	22	22	46	46	46	46	8	8
Si	3.02	3.04	5.45	5.45	5.48	6.20	6.21	6.14	8.05	7.95	8.00	7.70	2.89	2.90
Ti	0.00	0.00	0.28	0.27	0.23	0.06	0.04	0.04	0.17	0.15	0.13	0.10	0.00	0.00
Al	1.98	1.95	3.41	3.43	3.56	5.53	5.55	5.64	17.23	17.43	17.44	17.87	1.09	1.11
Cr	0.00	0.00	0.00	0.01	0.00	0.00	0.01	0.00	0.02	0.00	0.01	0.01	0.00	0.00
Fe	2.11	2.10	2.31	2.35	2.21	0.11	0.10	0.09	2.81	2.82	2.78	2.81	0.01	0.01
Mn	0.47	0.52	0.02	0.03	0.02	0.00	0.01	0.00	0.11	0.10	0.12	0.11	0.00	0.00
Mg	0.35	0.32	2.20	2.11	2.11	0.08	0.08	0.10	0.69	0.62	0.55	0.55	0.00	0.00
Zn									0.06	0.11	0.12	0.11		
Ca	0.05	0.04	0.00	0.00	0.00	0.00	0.00	0.00	0.00	0.00	0.00	0.00	0.10	0.08
Na	0.01	0.00	0.08	0.09	0.13	0.36	0.32	0.31	0.01	0.00	0.04	0.02	0.91	0.88
K	0.00	0.00	1.68	1.70	1.68	1.65	1.63	1.66	0.00	0.00	0.00	0.00	0.00	0.04
Total	**7.99**	**7.98**	**15.44**	**15.45**	**15.41**	**13.98**	**13.95**	**13.98**	**29.16**	**29.18**	**29.17**	**29.28**	**5.01**	**5.01**
X_{Mg}	0.14	0.13	0.49	0.47	0.49	0.44	0.45	0.51	0.20	0.18	0.16	0.16		
X_{Alm}	0.71	0.70												
X_{Pyr}	0.12	0.11												
X_{Sps}	0.16	0.17												
X_{Grs}	0.02	0.01												
X_{An}													0.10	0.08
X_{Ab}													0.90	0.89
X_{Or}													0.00	0.04

4. Results

4.1. Petrographic description

Field survey identified the main lithologies of the AVF as psammitic and pelitic schists, with minor phyllites and intercalated mafic or siliceous layers. The dominant foliation trends ENE-WSW to NE-SW, and dips toward the S to SE, consistent with the regional structure of the DLC (Fig. 1d). The psammitic and pelitic schists exhibit well-developed schistosity and layering or banding structures, alternating with one another (Fig. 2). Mafic or siliceous schists occur mainly as intercalated layers or small blocks within these host schists. Despite some subconcordant leucocratic veins cutting into the A Vuong schists (Figs. 2e-f), it remains uncertain whether these veins are related to the Dai Loc granitoids. The psammitic and pelitic metamorphic rocks are typically mica-rich and occasionally contain chlorite, garnet, staurolite, and kyanite as well as a rare occurrence of andalusite. Based on mineral assemblages and textures, they are likely to be divided into two groups: a low-grade group of phyllites (Fig. 3a) and fine-grained schists (Figs. 3b-f), and a high-grade group of medium-grained schists (Figs. 4a-c, g-i). The detailed petrography of the representative rock types is described below.

Figure 2. Representative outcrops for the analyzed samples from the A Vuong Formation. (a) Strongly weathered low-grade Ser phyllite (42606). (b) Layering Grt–Chl–Ms–Bt schist (42903C) intercalated with mafic schist. (c) Grt–Bt–Ms schist (42705A) intercalated with psammitic schist. (d) Visible dark red Grt porphyroblast in the close-up photo of Grt–Bt–Ms schist (42705A). (e) Ky–St–And–Bt–Ms schist (42803A) intruded by subconcordant Qz veins. (f) Grt–St–Bt–Ms schist (43007A) associated with leucocratic veins and interlayered with Grt–Bt schist (43007B)

4.1.1. Sericite phyllite

This is composed primarily of sericite, carbonaceous materials, and quartz, which is usually present as a matrix mineral. Feldspars (K-feldspar or plagioclase) are likely to have been altered to sericite. The metamorphic foliation in this rock is defined by the compositional banding of fine-grained sericite and carbonaceous materials (Fig. 3a), giving the rock a slightly dark and shiny appearance.

4.1.2. Chlorite schist

This rock exhibits microfolding and contains chlorite and significant carbonaceous materials (Fig. 3b), giving the rock a darker, metallic luster. Quartz and muscovite are commonly present as well. Carbonaceous materials appear as fine-grained disseminated flakes, small aggregates, or distinct layers in the matrix. Anhedral green chlorite typically forms fine-grained, platy, or flaky crystals. Accessory muscovite occurs as fine-grained, colorless flakes that align with the preferred orientation.

4.1.3. Biotite-muscovite-chlorite schist

Occurring as the most common schist in the study area, this rock type contains chlorite, biotite, muscovite, plagioclase, and quartz as the main mineral assemblage (Figs. 3c-d). Plagioclase occurs as a spotted porphyroblast, which is often accompanied by a fine-grained chlorite or muscovite pressure shadow (Fig. 3c). The preferred orientation of muscovite, chlorite, and biotite defines the pronounced foliation. The alignment of carbonaceous materials marks occasional crenulation cleavage (Fig. 3d). Zircon, apatite, and opaque minerals, including carbonaceous materials, are common accessory minerals.

4.1.4. Garnet-chlorite-biotite-muscovite schist

This schist mainly consists of chlorite, biotite, muscovite, garnet, quartz, plagioclase, and K-feldspar, with minor opaque minerals, zircon, monazite, and apatite (Fig. 3e). Chlorite, biotite, and muscovite appear as platy or flaky crystals, with the preferred orientation creating a well-developed schistose texture. Fine-grained, rounded to dodecahedral garnet, accompanied by cracks or fractures filled with chlorite or K-feldspar, is embedded in a finer-grained matrix. It contains inclusions of quartz, chlorite, and opaque minerals. Anhedral plagioclase and K-feldspar are partly altered to sericite.

4.1.5. Kyanite-bearing muscovite siliceous schist

This schist is enriched in quartz, with subordinate muscovite and kyanite, which exhibit a preferred orientation (Fig. 3f). Thin films of muscovite surround anhedral kyanite grains. The accessory minerals include opaque minerals, tourmaline, zircon, and apatite (Fig. 3f).

4.1.6. Staurolite-kyanite-biotite-muscovite ± andalusite ± garnet schist

This schist is made up of staurolite, kyanite, biotite, muscovite, and quartz as the main mineral assemblage, with minor amounts of plagioclase, graphite, and occasional andalusite or garnet (Figs. 4a-c). Accessory minerals include rutile, ilmenite, pyrite, tourmaline, apatite, xenotime, zircon, and monazite. The alignment of biotite and muscovite defines the schistosity. Staurolite and kyanite occur as aggregates or porphyroblasts, with subhedral to euhedral prismatic staurolite, and bladed or elongated kyanite crystals. Some staurolite grains show intergrowths with quartz. Biotite and muscovite usually form as platy, flaky crystals that are intergrown with each other (Figs. 4a-c). Minor garnet occasionally appears as an anhedral to subhedral porphyroblast, containing staurolite and quartz inclusions (Fig. 4a). Fine-grained kyanite is also found in direct contact with the garnet rim. Andalusite occurs in only one sample as subhedral,

prismatic, or blocky porphyroblasts (Figs. 4b-c). This porphyroblast includes muscovite, biotite, quartz, sillimanite, kyanite, staurolite + quartz, and monazite, and is rimmed by elongated or bladed kyanite crystals (Figs. 4b-c). These aluminosilicate minerals were identified not only by optical characteristics but also by Raman spectra (Figs. 4d-f). Secondary muscovite and chlorite are also present.

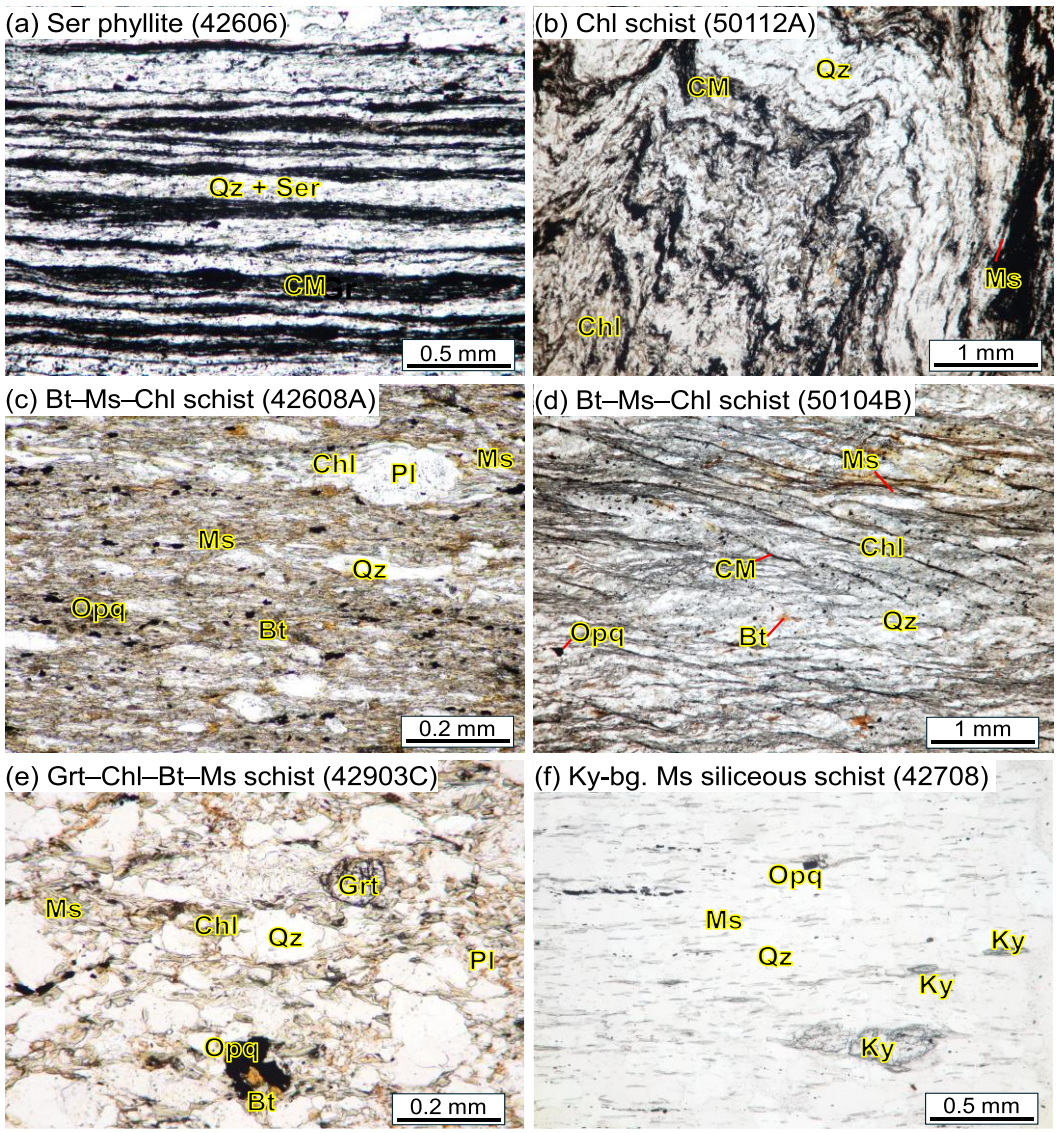

Figure 3. Photomicrographs of representative low-grade samples from the A Vuong Formation. (a) The alternation of Qz + Ser layers and CM layers forms fine-grained schistosity of Ser phyllite (42606). (b) Disseminated flakes of Chl follow microfolding in Chl schist (50112A). (c) Pl occurs as a spotted porphyroblast in Bt–Ms–Chl schist (42608A). (d) The CM is oriented along the crenulation cleavage, and lepidoblastic Bt, Ms, and Chl are folded in the Bt–Ms–Chl schist (50104B). (e) Dodecahedral Grt embedded in a fine-grained matrix in Grt–Chl–Bt–Ms schist (42903C). (f) Fine-grained Ky and Ms show a preferred orientation in Ky-bg. Ms siliceous schist (42708). CM: carbonaceous materials

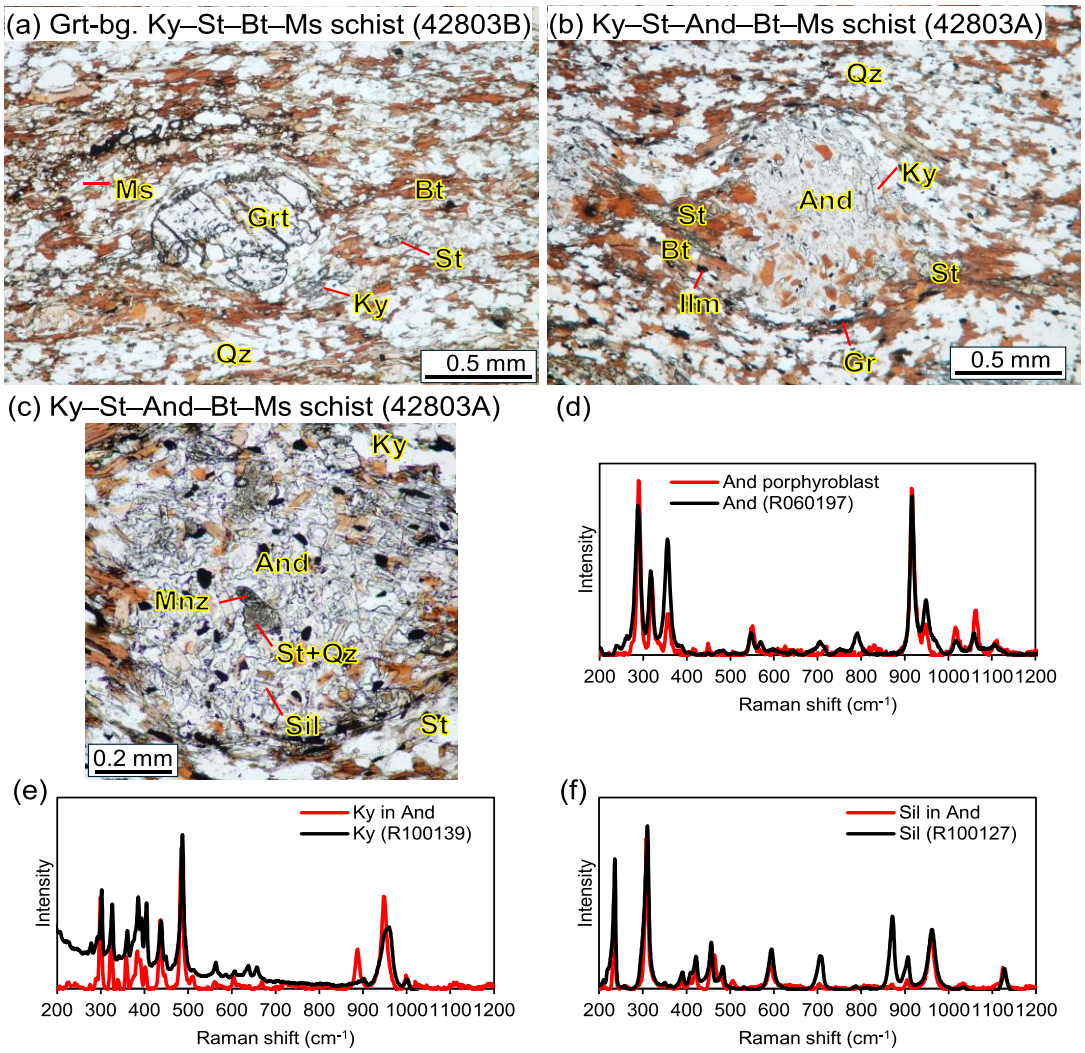

Figure 4. Photomicrographs of representative high-grade schists from the A Vuong Formation (a-c, g-i) and Raman spectra of And, Ky and Sil in sample 42803A (d-f). (a) Bt and Ms wrap Grt porphyroblast in Grt-bg. Ky–St–Bt–Ms schist (42803B). (b-c) Porphyroblastic And is rimmed by elongated or bladed Ky and includes Ky, Sil and St + Qz in Ky–St–And–Bt–Ms schist (42803A). (d) Raman spectrum of an And porphyroblast in 42803A fits with the reference one of RRUFFID R060197. (e) The Raman spectrum of a Ky inclusion in And of 42803A matches the reference spectrum of RRUFFID R100139. (f) The Raman spectrum of a Sil inclusion in And of 42803A matches the reference spectrum of RRUFFID R100127. (g) Euhedral Grt and subhedral St porphyroblasts have an inclusion-rich core and almost free inclusion thin rim in Grt–St–Bt–Ms schist (43007A). (h) Subhedral zoned Grt porphyroblast occurs in Grt–Bt schist (43007B). (i) Grt porphyroblast with three distinct domains of inclusion-rich core, inclusion-free mantle and dusty rim in Grt–Bt–Ms schist (42705B)

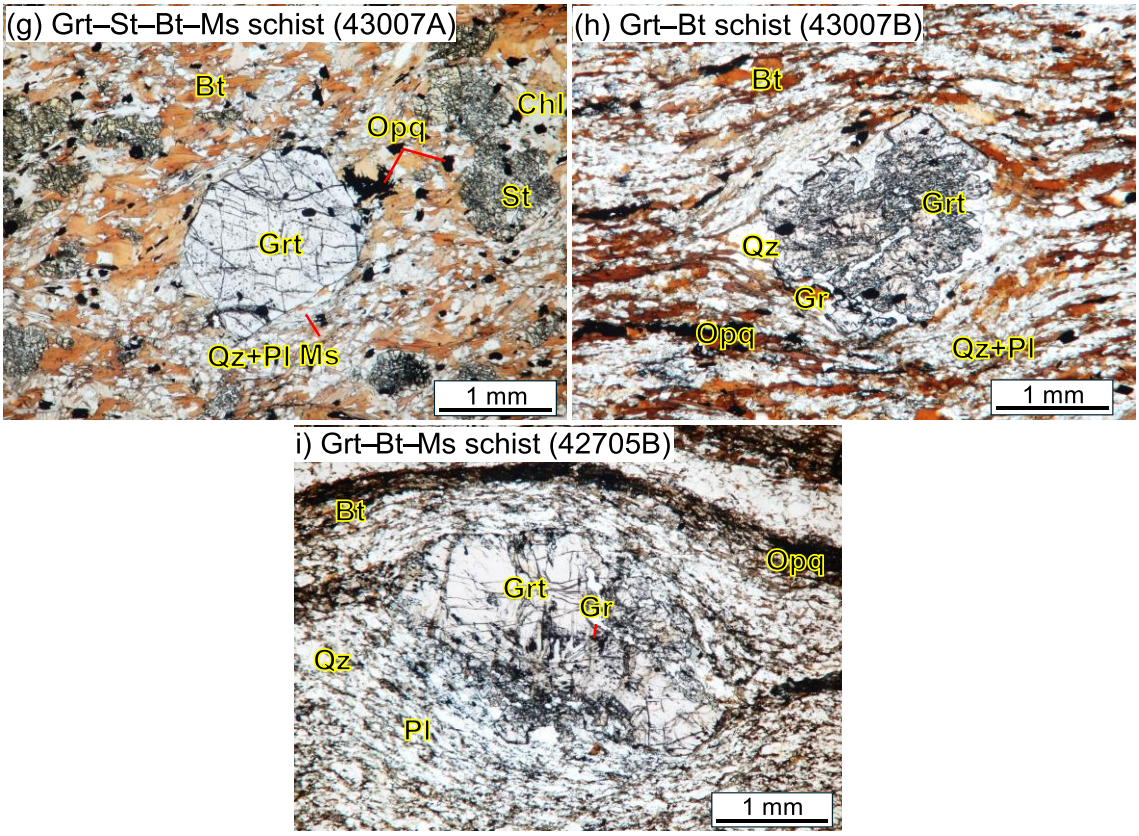

Figure 4. Cont.

4.1.7. Garnet-staurolite-biotite-muscovite schist

This schist contains mainly garnet, staurolite, biotite, muscovite, quartz, and plagioclase, as well as opaque minerals such as ilmenite, pyrite, pyrrhotite, and accessory minerals of tourmaline, rutile, zircon, and apatite (Fig. 4g). Euhedral porphyroblastic garnet displays a well-developed core-rim texture. The main core contains spiral or curved inclusions trails of quartz, plagioclase, ilmenite, rutile, tourmaline, and other tiny unidentified phases, while the thin rim is almost inclusion-free (Fig. 4g). Staurolite features a quartz inclusion-rich dusty core, an inclusion-poor rim and is partially replaced by secondary chlorite (Fig. 4g). Platy or flaky biotite and muscovite crystals are commonly aligned along the foliation.

4.1.8. Garnet-biotite ± muscovite schist

This schist is occasionally interlayered with staurolite-bearing schist (Fig. 2f) and includes garnet as a subhedral, coarse-grained porphyroblast within the finer-grained matrix of aligned biotite, muscovite, and quartz (Figs. 4h-i). The garnet porphyroblast grows unevenly, showing a distinct zoned pattern: an inclusion-rich core displaying sector zoning, with the inclusions trails of quartz, plagioclase, and opaque minerals, followed by an inclusion-poor rim (Figs. 4h-i). Accessory minerals include tourmaline, zircon, monazite, apatite, and opaque minerals, including graphite. Secondary minerals of chlorite, muscovite, and sericite are also observed.

4.2. Mineral chemistry

As a representative high-grade sample, the garnet-bearing kyanite-staurolite-biotite-muscovite schist (42803B) was selected for chemical analyses of garnet, staurolite, biotite, muscovite, and plagioclase to estimate the *P-T* conditions.

The elemental maps of garnet indicate an almost homogeneous chemical zoning, except for Ca, which shows a decreasing trend toward the grain margins (Fig. 5). In the high-Ca domain [X_{Grs} = Ca/(Fe + Mn + Mg + Ca) = 0.03], X_{Mg} [= Mg/(Mg + Fe)] values range from 0.134 to 0.138. In the low-Ca domain (X_{Grs} = 0.01–0.02), X_{Mg} values are more scattered, between 0.131 and 0.143 (Fig. 6a). X_{Sps} [= Mn/(Fe + Mn + Mg + Ca)] values for the former and latter are 0.16 and 0.15–0.17, respectively.

The analyzed biotite occurs in the matrix, in contact with either fine-grained staurolite around garnet, with muscovite or with a kyanite + staurolite + quartz intergrowth. Their Ti concentrations show slight variations depending on their occurrences (Fig. 6b). The highest Ti concentration, 0.28 (apfu) based on 22 oxygen numbers, was obtained from biotite near fine-grained staurolite, with X_{Mg} = 0.49. Those of biotite in contact with muscovite are 0.23–0.27 (apfu), with X_{Mg} = 0.47–0.50. The lowest Ti contents, 0.21–0.23 (apfu), are observed in biotite associated with kyanite and a staurolite + quartz intergrowth, accompanied by X_{Mg} values of 0.48–0.49.

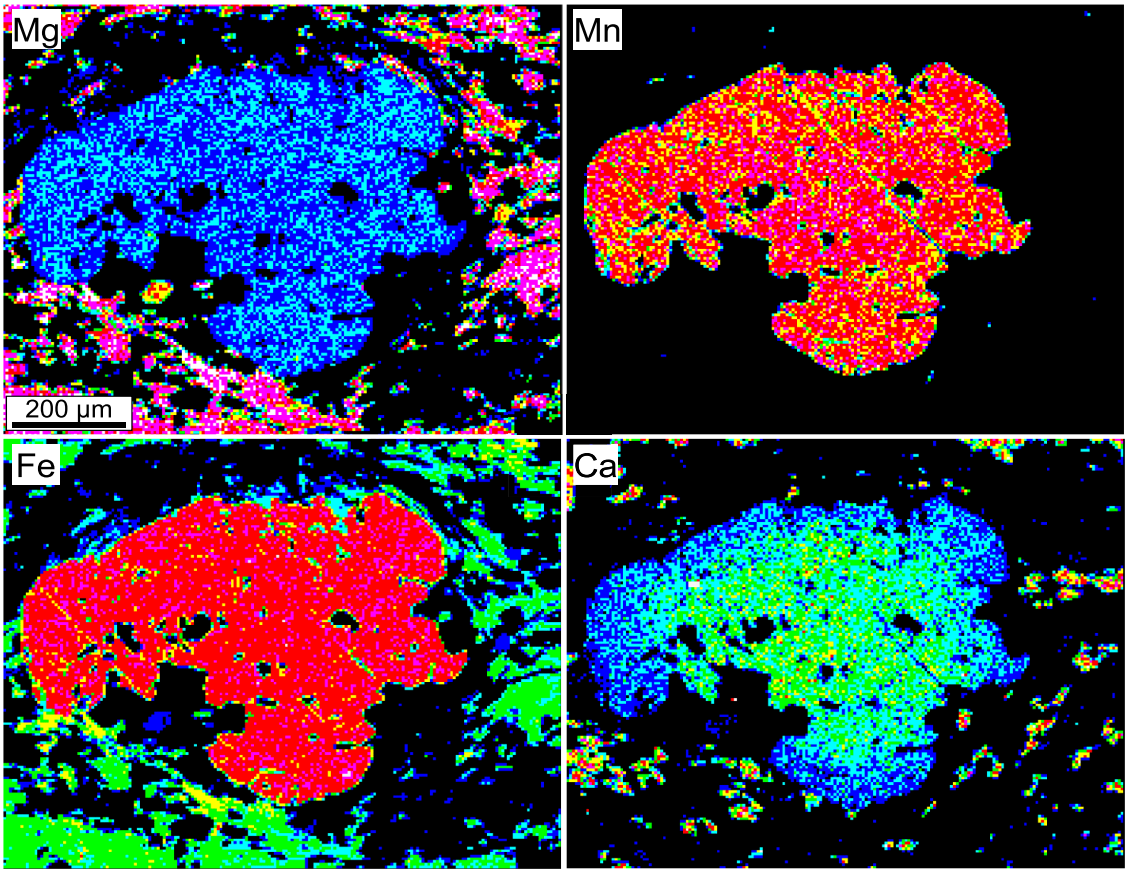

Figure 5. X-ray elemental maps for Mg, Mn, Fe and Ca of Grt in Grt-bg. Ky–St–Bt–Ms schist (42803B). The Ca contents slightly decrease toward the margin

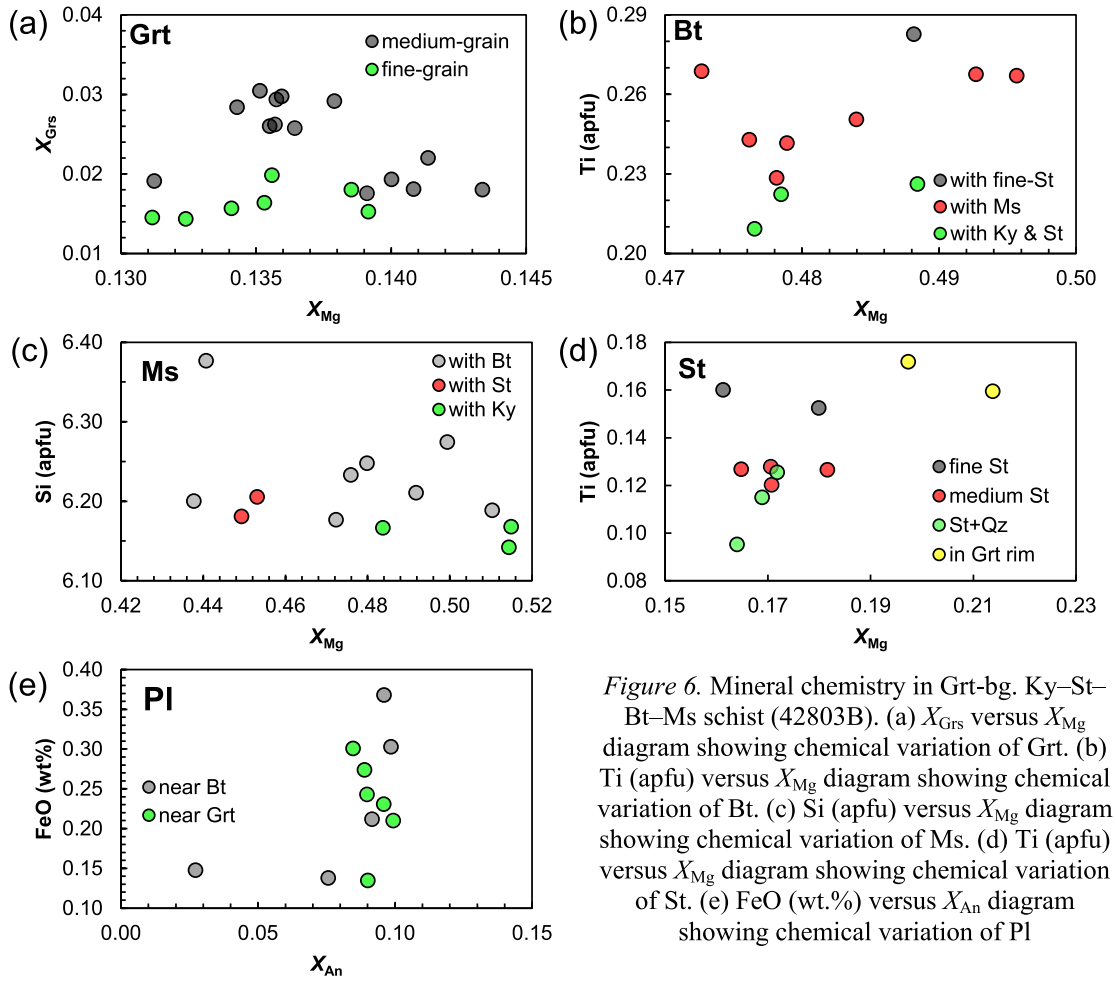

Figure 6. Mineral chemistry in Grt-bg. Ky–St–Bt–Ms schist (42803B). (a) X_{Grs} versus X_{Mg} diagram showing chemical variation of Grt. (b) Ti (apfu) versus X_{Mg} diagram showing chemical variation of Bt. (c) Si (apfu) versus X_{Mg} diagram showing chemical variation of Ms. (d) Ti (apfu) versus X_{Mg} diagram showing chemical variation of St. (e) FeO (wt.%) versus X_{An} diagram showing chemical variation of Pl

Muscovite grains associated with kyanite exhibit lower Si contents of 6.14–6.17 (apfu), based on 22 oxygen numbers, and higher X_{Mg} values of 0.48–0.51 (Fig. 6c). In contrast, muscovite associated with a staurolite + quartz intergrowth shows slightly higher Si contents of 6.18–6.21 (apfu) and X_{Mg} value of 0.45. The muscovite in contact with biotite is characterized by elevated Si contents of 6.18–6.38 (apfu) and more variable X_{Mg} values of 0.44–0.51.

Chemical compositions of staurolite display similar trends to those observed in biotite (Fig. 6d). Fine-grained euhedral staurolite in contact with biotite near garnet has X_{Mg} values of 0.16–0.18 and higher Ti concentrations of 0.15–0.16 (apfu), based on 46 oxygen numbers, compared to the medium-grained, subhedral staurolite aggregates [X_{Mg} = 0.16–0.18 and Ti = 0.12–0.13 (apfu)]. The anhedral staurolite + quartz intergrowth associated with kyanite aggregates shows lower low Ti concentrations (0.10–0.13 apfu) and X_{Mg} values of 0.16–0.17. Staurolite inclusions in the garnet rim display the highest X_{Mg} (0.20–0.21) and Ti contents (0.16–0.17 apfu), and lower Zn contents (0.06–0.08 apfu) than others (0.09–0.13 apfu) (Table 1).

Plagioclase occurs in the matrix and exhibits no systematic chemical difference based on its textural occurrences (Fig. 6e). The anorthite contents [X_{An} = Ca/(Ca + Na + K)] of plagioclase range mainly from 0.08 to 0.10, with a few analyses yielding lower values around 0.03.

5. Discussions

5.1. Metamorphic zonation and progressive metamorphism

The dominant foliation (Fig. 1d) and microfolding structures (Figs. 3b, d) observed in the phyllites and schists of the AVF in this study are consistent with previous descriptions by Faure et al. (2018), who reported weakly metamorphosed quartz–sericite schist, sandstone, and quartzite in this formation. However, this study additionally identified the distributions of not only low-grade metamorphic rocks (Fig. 3) but also high-grade ones (Figs. 4a-c, g-i). Based on thorough petrographic observation, two metamorphic zones, a biotite-chlorite zone (Bt–Chl zone) and a staurolite zone (St zone) were defined based on the unique texture and mineral assemblages in pelitic to psammitic metamorphic rocks (Fig. 1c).

The Bt–Chl zone was defined by the occurrence of the low-grade group, including phyllite (Fig. 2a) and fine-grained schists containing chlorite and/or biotite (Fig. 3). This zone broadly covers the study area (Fig. 1c). Rocks in the Bt–Chl zone are characterized by fine-grained textures, microfolding, and mineral assemblages dominated by sericite or muscovite, chlorite and/or biotite, with minor garnet (Fig. 3). Paragenesis indicates a typical greenschist-facies grade. Rare kyanite coexisting with muscovite and quartz was also identified in a fine-grained siliceous schist (Fig. 3f). The metamorphic grade within the Bt–Chl zone ranges from lower greenschist-facies (biotite-free phyllites) to upper greenschist-facies (biotite-bearing schists) (Fig. 3). This variation may reflect a continuous reaction over a broad temperature range, as follows:

Chlorite + phengitic muscovite → muscovite + biotite + quartz + water

The St zone is spatially restricted to the central part of the AVF and is located near the Dai Loc granitoid body (Fig. 1c). The schists in this zone represent higher-grade metamorphic rocks, characterized by fine- to coarse-grained, euhedral to subhedral staurolite and/or garnet porphyroblasts exhibiting textural zonation (Figs. 4a-c, g-i). These rocks also contain fine- to medium-grained kyanite, biotite, muscovite, and quartz, with minor plagioclase and K-feldspar. The alignment of biotite and muscovite defines the foliation of schists. Rare andalusite porphyroblasts rimmed by kyanite crystals were observed in one schist sample (Fig. 4c). Their mineral assemblages reflect an amphibolite-facies metamorphic grade. The appearance of staurolite and disappearance of chlorite from the Bt–Chl zone to the St zone may suggest the following reaction:

Chlorite + muscovite ± garnet → staurolite + biotite + quartz + water

This reaction may have occurred in response to increasing temperature due to the steep positive P/T slope (e.g., Spear et al., 1999). Secondary chlorite and muscovite after staurolite and biotite (Fig. 4g) might have formed by a retrograde back-reaction during the cooling stage.

5.2. Metamorphic condition for staurolite zone in the A Vuong Formation

Several geothermobarometers were utilized for P-T estimation, including garnet-

biotite thermometers (Thompson, 1976; Holdaway and Lee, 1977; Ferry and Spear, 1978), garnet-staurolite thermometer (Perchuk, 1991), garnet-muscovite thermometer (Wu and Zhao, 2006), Ti-in-biotite thermometers (Henry et al., 2005; Wu and Chen, 2015), and barometers with coexisting pairs of garnet-biotite-muscovite-kyanite-plagioclase-quartz-rutile-ilmenite (Bohlen et al., 1983; Hoisch, 1990; Wu and Zhao, 2006; Wu, 2017, 2020). The GASP barometer was not employed due to low-Ca contents in garnet and plagioclase, as suggested by Holdaway (2001). A summary of the estimated results is provided in Table 2.

Table 2. Thermobarometric results

Method/Stage	**Peak**		**Retrograde**	
Thermometry (°C)				
Grt–Bt (Thompson, 1976)	609	623	566	580
Grt–Bt (Holdaway and Lee, 1977)	590	597	553	559
Grt–Bt (Ferry and Spear, 1978)	596	603	541	548
Grt–St (Perchuk, 1991)	603	607	534	539
Grt–Ms (Wu and Zhao, 2006)	588	588	550	550
Ti in Bt (Henry et al., 2005)	638	638	610	610
Ti in Bt (Wu and Chen, 2015)	600	619	586	604
Reference P (kbar)	*5*	*7*	*5*	*7*
Barometry (kbar)				
GRAIL (Bohlen et al., 1983)	7.8	8.9	6.5	7.5
BMRAIL (Wu, 2020)	6.9	9.2	4.6	7.0
GBAS_P1 (Wu, 2017)	7.1	9.2	5.3	7.1
GBAS_P2 (Wu, 2017)	7.0	9.8	4.5	7.2
GBPS_P1 (Hoisch, 1990)	5.9	7.4	4.5	6.0
GBPS_P2 (Hoisch, 1990)	5.9	7.9	4.3	6.3
GMPS_P1 (Wu and Zhao, 2006)	6.2	7.8	4.3	5.9
GMPS_P2 (Wu and Zhao, 2006)	5.8	8.0	3.7	6.0
Reference T (^{O}C)	*600*	*700*	*500*	*600*

The peak *P*-*T* condition of *ca.* 5.5–8.7 kbar and 590–640°C were calculated for a garnet-bearing kyanite-staurolite-biotite-muscovite schist (42803B) from the St zone (Fig. 7). These estimations were derived using chemical compositions of high-X_{Mg} rim in medium-grained garnet, low-X_{Mg} biotite and muscovite, high-X_{An} plagioclase surrounding the garnet, and low-X_{Mg} fine-grained staurolite. The calculated metamorphic condition falls within the stability fields of both kyanite and staurolite + quartz, as well as the assemblages of staurolite + biotite + quartz and muscovite + albite + H_2O (Fig. 7), which aligns well with the petrographic features of sample 42803B. This schist occurs together with andalusite-bearing pelitic schist (42803A), in which andalusite including kyanite, sillimanite, and staurolite + quartz is overgrown by kyanite (Fig. 4c). Thus, these observations suggest that the pelitic schists experienced low-*P*/*T* metamorphism under equilibrium conditions at the triple point of andalusite–kyanite–sillimanite during the prograde stage (Fig. 7). Such low-*P*/*T* conditions may have been locally induced by the intrusions of subconcordant leucocratic veins (Figs. 2e-f), possibly related to the Dai Loc granitoids or other intrusions from the Hai Van or Ben Giang-Que Son Complexes, as previous reported, into the AVF schists. Subsequent compression and heating may have led these schists to the peak metamorphic condition of *ca.* 5.5–8.7 kbar and 590–640°C under the kyanite stability field (Fig. 7). The condition for the retrograde stage was also estimated at *ca.* 4.4–7.4 kbar and 530–570°C by using chemical compositions of low-X_{Mg} fine-grained garnet, high-X_{Mg} biotite and muscovite near kyanite, low-X_{An} plagioclase around the garnet, and high-X_{Mg} fine-grained staurolite. This condition is located on the lower temperature side of the above isograd reaction for the St zone, supporting the formation of secondary chlorite and muscovite in this zone through retrograde back-reactions. Combining all metamorphic conditions for the prograde, peak, and retrograde stages with no replacement of kyanite by sillimanite for this schist implies an anti-clockwise *P*–*T* trajectory rather than a clockwise one accompanied by post-peak decompression (Fig. 7).

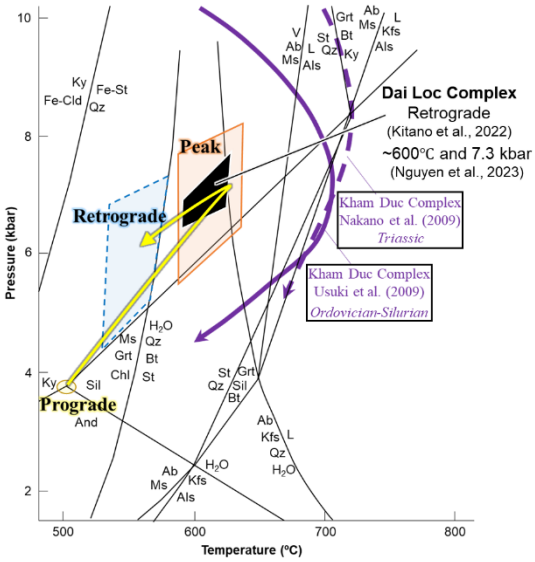

Figure 7. Estimated *P-T* conditions for Grt-bg. Ky–St–Bt–Ms schist (42803B) from the St zone. The clockwise *P-T* paths for the Kham Duc Complex, Kontum Massif, suggested by Nakano et al. (2009) and Usuki et al. (2009) are also shown with purple dashed and solid arrows, respectively. The amphibolite-facies condition of the Dai Loc Complex reported by Kitano et al. (2022) and Nguyen et al. (2023) is also present. The *P-T* grids are after Le Breton and Thompson (1988), Spear and Cheney (1989), and Spear et al. (1999). The peak *P-T* condition of the schist (42803B) is comparable with the amphibolite-facies one of the Dai Loc Complex but not with the Kham Duc Complex. Moreover, the *P-T* trajectory tends to be anti-clockwise

5.3. Metamorphic correlation with neighboring metamorphic rocks and their geological implications

The occurrences of similar medium-*P*/*T* series metamorphic rocks, such as kyanite-bearing garnet-staurolite-biotite schist, have been reported from the Kham Duc Complex in the KTM, south of the TKPS shear zone (e.g., Osanai et al., 2008; Nakano et al., 2009; Usuki et al., 2009) (Fig. 1b). These schists exhibit a clockwise *P-T* path with peak conditions at *ca.* 7–8 kbar and 730–750°C during the Triassic (Nakano et al., 2009), or 6.8–7.0 kbar and 711–722°C during the Ordovician-Silurian under the sillimanite stability field (Usuki et al., 2004, 2009) (Fig. 7). The clockwise *P–T* paths were inferred petrographically from the overgrowth of sillimanite around kyanite (Nakano et al., 2009; Usuki et al., 2009), the presence of cordierite + spinel symplectites after sillimanite + gedrite, and secondary andalusite containing relic kyanite (Nakano et al., 2009). However, these petrological characteristics of the Kham Duc Complex are in contrast with the St zone in the AVF, particularly in terms of the sillimanite-stable peak metamorphic condition and the decompression-dominated, clockwise *P-T* path crossing the sillimanite stability field. Alternatively, pelitic gneisses in the DLC surrounding the AVF experienced kyanite-stable amphibolite-facies condition following earlier sillimanite-stable granulite-facies metamorphism at *ca.* 430–450 Ma (Bui et al., 2022; Kitano et al., 2022; Nguyen et al., 2023). However, the timing of the kyanite-stable metamorphism remains uncertain and debated (Bui et al., 2022, 2023; Nguyen et al., 2023). Kyanite-grade *P-T* conditions were estimated at *ca.* 7.3 kbar and 600°C as part of a possible Triassic metamorphic cycle (Nguyen et al., 2023), or *ca.* 6.5–7.8 kbar and 580–630°C as part of an early Devonian retrograde stage following granulite-facies metamorphism (Kitano et al., 2022; Bui et al., 2023). These conditions are likely comparable with the peak metamorphic condition identified in the AVF (Fig. 7), suggesting a potential tectono-thermal linkage. Nevertheless, it is essential to clarify whether amphibolite-facies metamorphism in the AVF and DLC occurred synchronously. A candidate for the timing is probably the early Devonian or Triassic, according to the metamorphic ages of medium-*P*/*T* metamorphism in the DLC reported by Bui

et al. (2023) and Nguyen et al. (2023). The former is relatively minor thermal events in the Indochina Block, while the latter correlates with the well-known Indosinian orogeny. Therefore, constraining the metamorphic age of the AVF is crucial not only for understanding its tectonic relationship with the DLC, but also for deciphering the tectonic evolution of the southern TSB. Taking previous studies into account, the peak amphibolite-facies metamorphism in the AVF may have taken place after the maximum depositional age of 516 Ma of from detrital zircons (Wang et al., 2016), and may have been influenced by local contact metamorphism associated with late Ordovician to early Devonian intrusions (e.g., Carter et al., 2001; Bui et al.., 2022; Nguyen et al., 2023), such as the Dai Loc granitoids (Thuc et al., 1995; Tran and Vu, 2011). Intriguingly, this study revealed a distinctive anti-clockwise *P*-*T* path in the high-grade schist of the AVF, southern TSB (Fig. 7), in contrast to the typical clockwise paths associated with Permian-Triassic collision-induced metamorphism observed throughout the TSB and KTM (e.g., Osanai et al., 2008; Faure et al., 2018). This new finding may imply that the AVF may have experienced a tectono-thermal history distinct from the major Permian-Triassic collisional events that generated high-grade rocks along the regional shear zones (Fig. 1a). Thus, further petrochronological studies of the AVF could play an important role in providing new insights into not only the tectonic link between the AVF and DLC, but also the broader tectonic evolution of the southern TSB.

In summary, our preliminary geological survey and petrographic analysis revealed metamorphic zonation in the AVF, ranging from the greenschist- to amphibolite-facies, along the medium-*P*/*T* series. The results reflect a complex history of tectonic burial and exhumation, possibly linked to tectonic process affecting the adjacent DLC. Further petrological and geochronological studies are essential to reconstruct the tectono-thermal history of this formation accurately. Such efforts will enhance our understanding of not only the metamorphic evolution of the TSB but also the broader tectonic framework of Southeast Asia.

6. Conclusions

This study presents the first comprehensive petrographic and metamorphic characterization of the AVF, revealing a metamorphic zonation from lower greenschist-facies phyllites to amphibolite-facies schists corresponding to the biotite-chlorite and staurolite zones. Employing conventional geothermobarometry, the analyzed high-grade schist containing garnet, kyanite, and staurolite in the staurolite zone records a peak metamorphic condition at *ca.* 5.5–8.7 kbar and 590–640°C, followed by retrograde metamorphism at *ca.* 4.4–7.4 kbar and 530–570°C. The occurrence of andalusite porphyroblasts, including sillimanite and kyanite, rimmed by kyanite, in a pelitic schist interlayered with the analyzed schist, indicates equilibrium of andalusite-sillimanite-kyanite and a later transition to kyanite-stable condition during the prograde stage. These results, combined with the absence of sillimanite overgrowing kyanite, indicate an anti-clockwise *P*-*T* trajectory for the A Vuong schists. The unique *P*-*T* condition and path of the AVF are clearly inconsistent with those of the adjacent medium-*P*/*T* metamorphic rocks of the Kham Duc Complex in the KTM but are potentially consistent with the amphibolite-facies metamorphic stage observed in the neighboring DLC. This suggests a possible tectonic linkage between the AVF and DLC, although further geochronological investigations are required to confirm whether their developments were synchronous.

Acknowledgements

We appreciate two anonymous reviewers for their constructive and valuable comments, and the VJES editor Phan T.T. for smooth editorial handling. Matsumoto A. is thanked for her help with the electron microprobe analysis. We deeply thank Otake T. and Kikuchi R. for allowing us to use the Raman spectroscopy and scanning electron microscope. The special thanks are given to Edward A. for the significant English correction. This research was funded by Vietnam National Foundation for Science and Technology Development (NAFOSTED) under grant number 105.99-2023.10.

References

Bohlen S.R., Wall V.J., Boettcher A.L., 1983. Experimental investigations and geological applications of equilibria in the system FeO-TiO_2-Al_2O_3-SiO_2-H_2O. American Mineralogist, 68, 1049–1058.

Bui V.T.S., Osanai Y., Nakano N., Adachi T., Kitano I., Owada M., 2020. Timing of high-grade metamorphism in the Kontum Massif, Vietnam: Constraints from zircon-monazite multi-geochronology and trace elements geochemistry of zircon-monazite-garnet. Journal of Asian Earth Sciences, 187, 104084.

Bui T.S.V., Osanai Y., Nakano N., Kitano I., Adachi T., Tran T.A., Pham B., 2022. Petrology and zircon U–Pb geochronology of pelitic gneisses and granitoids from the Dai Loc Complex in the Truong Son Belt, Vietnam: Implication for the Silurian magmatic-metamorphic event. Journal of Asian Earth Sciences, 226, 105070.

Bui T.S.V., Kitano I., Osanai Y., Nakano N., 2023. Monazite dating of pelitic gneisses in the Dai Loc Complex, Truong Son Belt, Vietnam. International Association for Gondwana Research 2023 Convention and 20th International Conference on Gondwana to Asia, abstract, 78.

Carter A., Roques D., Bristow C., Kinny P., 2001. Understanding Mesozoic accretion in Southeast Asia: Significance of Triassic thermotectonism (Indosinian orogeny) in Vietnam. Geology, 29(3), 211.

Faure M., Nguyen V.V., Luong T.T.H., Lepvrier C., 2018. Early Paleozoic or Early-Middle Triassic collision between the South China and Indochina Blocks: The controversy resolved? Structural insights from the Kon Tum massif (Central Vietnam). Journal of Asian Earth Sciences, 166, 162–180.

Ferry J.M.T., Spear F.S., 1978. Experimental calibration of the partitioning of Fe and Mg between biotite and garnet. Contribution to Minerology and Petrology, 66(2), 113–117.

Gardner C.J., Graham I.T., Belousova E., Booth G.W., Greig A., 2017. Evidence for Ordovician subduction-related magmatism in the Truong Son terrane, SE Laos: Implications for Gondwana evolution and porphyry Cu exploration potential in SE Asia. Gondwana Research, 44, 139–156.

Henry D.J., Guidotti C.V., Thomson J.A., 2005. The Ti-saturation surface for low-to-medium pressure metapelitic biotites: Implications for geothermometry and Ti-substitution mechanisms. American Mineralogist, 90, 316–328.

Hoisch T.D., 1990. Empirical calibration of six geobarometers for the mineral assemblage quartz + muscovite + biotite + plagioclase + garnet. Contribution to Minerology and Petrology, 104, 225–234.

Holdaway M.J., Lee S.M., 1977. Fe-Mg cordierite stability in high-grade pelitic rocks based on experimental, theoretical, and natural observation. Contribution to Minerology and Petrology, 63, 175–198.

Holdaway M.J., 2001. Recalibration of the GASP geobarometer in light of recent garnet and plagioclase activity models and versions of the garnet-biotite geothermometer. American Mineralogist, 86, 1117–1129.

Hung C., 1996. Geological Map of Vietnam on scale 1:50.000. Hoi An-Da Nang sheet. South Vietnam Geological Mapping Division, General Department of Geology and Minerals of Vietnam.

Jiang W., Yu J.H., Wang X., Griffin W.L., Pham T.H., Nguyen D.L., Wang F., 2020. Early Paleozoic

magmatism in northern Kontum Massif, Central Vietnam: Insights into tectonic evolution of the eastern Indochina Block. Lithos, 376–377, 105750.

Kitano I., Bui T.S.V., Osanai Y., Nakano N., Pham B., Hokada T., 2022. The pressure-temperature conditions of high-grade pelitic gneisses in the Dai Loc Complex, Truong Son Belt, central Vietnam. The Thirteenth Symposium on Polar Science, abstract.

Le Breton N., Thompson A.B., 1988. Fluid-absent (dehydration) melting of biotite in metapelites in the early stages of crustal anatexis. Contributions to Mineralogy and Petrology, 99, 226–237.

Lepvrier C., Maluski H., Nguyen V.V., Roques D., Axente V., Rangin C., 1997. Indochina NW-trending shear zones within the Truong Son belt (Vietnam): ^{40}Ar-^{39}Ar Triassic ages and Cretaceous to Cenozoic overprints. Tectonophysics, 283, 105–127.

Lepvrier C., Maluski H., Vu V.T., Leyreloup A., Thi P.T., Nguyen V.V., 2004. The Early Triassic Indosinian orogeny in Vietnam (Truong Son Belt and Kontum Massif): implications for the geodynamic evolution of Indochina. Tectonophysics, 393(1–4), 87–118.

Luong T.T.H., Nguyen V.V., Faure M., Wei L., Vu T.T., Tran T.T.N., Nguyen T.M.T., 2024. From rifting to Indosinian orogeny recorded in the Indochina from late Devonian to late Triassic: A review. Vietnam Journal of Earth Sciences, 47(1), 59–89.

Nagy E.A., Maluski H., Lepvrier C., Schärer U., Thi P.T., Leyreloup A., Thich, V.V., 2001. Geodynamic significance of the Kontum massif in central Vietnam: composite ^{40}Ar/^{39}Ar and U–Pb ages from Paleozoic to Triassic. The Journal of Geology, 109, 755–770.

Nakano N., Osanai Y., Owada M., Nam T.N., Tsunogae T., Toyoshima T., Binh P., 2004. Decompression process of mafic granulite from eclogite to granulite facies under ultrahigh-temperature condition in the Kontum massif, central Vietnam. Journal of Mineralogy and Petrological Sciences, 99, 242–256.

Nakano N., Osanai Y., Owada M., Nam T.N., Toyoshima T., Binh P., Tsunogae T., Kagami H., 2007. Geologic and metamorphic evolutions of the basement complexes in the Kontum Massif, central Vietnam. Gondwana Research, 12, 438–453.

Nakano N., Osanai Y., Owada M., Hayasaka Y., Nam T.N., 2009. Permo-Triassic Barrovian-type metamorphism in the ultrahigh-temperature Kontum Massif, central Vietnam: constraints on continental collision tectonics in Southeast Asia. The Island Arc, 18(1), 126–143.

Nakano N., Osanai Y., Owada M., Nam T.N., Charusiri P., Khamphavong K., 2013. Tectonic evolution of high-grade metamorphic terranes in central Vietnam: Constraints from large-scale monazite geochronology. Journal of Asian Earth Sciences, 73(5), 520–539.

Ngo X.T., Hung N.Q., Kim Y., Kwon S., Bui V.H., Tran T.H., Jang Y., Samuel V.O., 2024. Cambrian-Ordovician Arc-Related Magmatism in the Central Southeast Asian Continents and Its Significance on Early Palaeozoic Tectonics of the Indochina Block. Geological Journal, 60, 776–791.

Ngo X.T., Luong Q.K., Bui V.H., Tran T.H., Nguyen Q.H., Dinh T.T., 2025. Petrogenesis and geological significance of the early Paleozoic S-Type granitic mylonite in the Southwestern Kon Tum Massif, Central Vietnam. Vietnam Journal of Earth Sciences, 47(3), 1–18.

Nguyen D.N., Lo C.H., Usuki T., Iizuka Y., Pham B., 2023. P–T–t conditions of Early Palaeozoic low-P high-T granulitefacies metamorphism in the southern Truong Son Belt, Central Vietnam. Journal of Metamorphic Geology, 41, 1081–1117.

Nguyen H.T., Zong K., Liu Y., Yuan Y., Pham T.H., Le T.D., Pham M., 2021. Early Paleozoic arc magmatism and accretionary orogenesis in the Indochina Block, Southeast Asia. The Journal of Geology, 129(1), 33–48.

Nguyen Q.M., Feng Q., Zi J.-W., Zhao T., Tran H.T., Ngo T.X., Tran D.M., Nguyen H.Q., 2019. Cambrian intra-oceanic arc trondhjemite and tonalite in the Tam Ky-Phuoc Son Suture Zone, central Vietnam: implications for the early Paleozoic assembly of the Indochina Block. Gondwana Research, 70, 151–170.

Nguyen T.B.T., Pham T.T.H., Xin Q., Bui T.A., Nguyen T.X., Pham M., Ho T.T., 2024. Zircon U-Pb Geochronology, Geochemistry, and Sr-Nd-Hf Isotopic Composition of Ben Giang-Que Son Complex in the Southern Truong Son Belt: Implications for Permian-Triassic Tectonic

Evolution. Minerals, 14, 569.

Nguyen V.T., 1995. Geological and Mineral resources map of Vietnam on scale 1:200.000. Huong Hoa-Hue-Da Nang sheet. Department of Geology and Minerals of Vietnam, Ha Noi.

Nguyen V.T., 1996a. Geological and Mineral resources map of Vietnam on scale 1:200.000. Ba Na sheet. Department of Geology and Minerals of Vietnam, Ha Noi.

Nguyen V.T., 1996b. Geological and Mineral Resources map of Vietnam on scale 1:200.000. Hoi An sheet. Department of Geology and Minerals of Viet Nam, Ha Noi.

Nguyen X.D., (Ed) 1996. Geological Maps on Scale 1:200.000 with Explanatory Note. Le Thuy-Quang Tri Sheet. Department of Geology of Vietnam, Hanoi.

Osanai Y., Nakano N., Owada M., Tran Ngoc Nam, Toyoshima T., Tsunogae T., Binh P., 2004. Permo-Triassic ultrahigh-temperature metamorphism in the Kontum massif, central Vietnam. Journal of Mineralogy and Petrological Sciences, 99, 225–241.

Osanai Y., Nakano N., Owada M., Tran N.N., Miyamoto T., Nguyen T.M., Nguyen V.N., Tran V.T., 2008. Collision zone metamorphism in Vietnam and adjacent Southeastern Asia: Proposition for Trans Vietnam Orogenic Belt. Journal of Mineralogical and Petrological Sciences, 103, 226–241.

Perchuk L.L., 1991. Derivation of a thermodynamically consistent set of geothermometers and geobarometers for metamorphic and magmatic rocks. In: Perchuk, L.L. (Ed.), Progress in Metamorphic and Magmatic Petrology: A Memorial Volume in Honor of D.S. Korzinskiy. Cambridge University Press, London, 93–111.

Pham T.H., Nguyen T.D., Nguyen T.B.T., Nguyen T.M., Pham M., 2016. U-Pb ages and Hf isotopic composition of zircon and bulk rock geochemistry of the Dai Loc granitoid complex in Kontum massif: Implications for Early Paleozoic crustal evolution in Central Vietnam. Journal of Mineralogical and Petrological Sciences, 111(5), 326–336.

Pham M., Pham T.H., Kawaguchi K., Nong T.Q.A., Le D.P., 2021. Geochemistry, zircon U-Pb geochronology and Sr-Nd-Hf isotopic composition of the Cha Val plutonic rocks in central Vietnam: Implications for Permian-Triassic Paleo-Tethys subduction-related magmatism. Vietnam Journal of Earth Sciences, 44(3), 301–326.

Sanematsu K., Murakami H., Duangsurigna S., Vilayhack S., Duncan R.A., Watanabe Y., 2011. $^{40}Ar/^{39}Ar$ ages of granitoids from the Truong Son fold belt and Kontum Massif in Laos. Journal of Mineralogical and Petrological Sciences, 106(1), 13–25.

Shang Z., Chen Y., 2022. Petrogenesis and Tectonic Implications of Early Paleozoic Magmatism in Awen Gold District, South Section of the Truong Son Orogenic Belt, Laos. Minerals, 12, 923.

Shi M.F., Lin F.C., Fan W.Y., Deng Q., Cong F., Tran M.D., Zhu H.P., Wang H., 2015. Zircon U-Pb ages and geochemistry of granitoids in the Truong Son terrane, Vietnam: Tectonic and metallogenic implications. Journal of Asian Earth Sciences, 101, 101–120.

Spear F.S., Cheney J.T., 1989. A petrogenetic grid for peliticschists in the system SiO_2-Al_2O_3-FeO-MgO-K_2O-H_2O. Contributions to Mineralogy and Petrology, 101, 149–16.

Spear F.S., Kohn M.J., Cheney J.T., 1999. P-T paths from anatectic pelites. Contributions to Mineralogy and Petrology, 134, 17–32.

Thassanapak H., Udchachon M., Burrett C., 2018. Silurian radiolarians from the Sepon Mine, Truong Son Terrane, central Laos and their palaeogeographic and tectonic significance. Geological Magazine, 155(8), 1621–1640.

Thompson A.B., 1976. Mineral reactions in pelitic rocks; II, Calculation of some PTX (Fe-Mg) phase relations. American Journal of Science, 276, 425–454.

Thuc D.D., Trung H., 1995. Geology of Vietnam II. Magma. Department of Geology of Vietnam, Hanoi, 359p (in Vietnamese).

Tran T.H., Tran T.A., Ngo T.P., Pham T.D., Tran V.A., 2005. Permian-Triassic magmatism of Vietnam and their potential of associated precious metals (Pt, Au), Proceedings of the scientific conference: 60th anniversary of Vietnam Geology, 63–79.

Tran T.H., Tran T.A., Ngo T.P., Pham T.D., Tran V.A., Izokh A.E., Borisenko A.S., Lan C.Y., Chung S.L., Lo C.H., 2008. Permo-Triassic intermediate-felsic magmatism of the Truong Son Belt, eastern margin

of Indochina. Comptes Rendus Geoscience, 340(2–3), 112–126.

Tran H.T., Zaw K., Halpin J.A., Manaka T., Meffre S., Lai C.K., Lee Y., Le H.V., Dinh S., 2014. The Tam Ky-Phuoc Son Shear Zone in central Vietnam: Tectonic and metallogenic implications. Gondwana Research, 26(1), 144–164.

Tran V.T., Vu K., 2011. Geology and earth resources of Viet Nam. Publish house for Science and Technology, 645p.

Tran T.V., Faure M., Nguyen V.V., Bui H.H., Fyhn M.B.W., Nguyen T.Q., Lepvrier C., Thomsen T.B., Tani K., Charusiri P., 2020. Neoproterozoic to Early Triassic tectono-stratigraphic evolution of Indochina and adjacent areas: A review with new data. Journal of Asian Earth Sciences, 191, 1–23.

Usuki T., Lan C.Y., Yeh M.W., Tran T.A., Iizuka Y., 2004, Metamorphic evolution in the northern Kontum Massif, central Vietnam. EOS Transactions, American Geophysical Union, 85(47), Fall Meeting Supplement, Abstract T11C-1273.

Usuki T., Lan C.Y., Yui T.F., Iizuka Y., Tich V.V., Anh T.T., Okamoto K., Wooden J.L., Liou J.G., 2009. Early Paleozoic medium-pressure metamorphism in central Vietnam: evidence from SHRIMP U-Pb zircon ages. Geoscience Journal, 13, 245–256.

Wang C., Liang X., Foster D.A., Fu J., Jiang Y., Dong C., Zhou Y., Wen S., Quynh P.V., 2016. Detrital zircon U-Pb geochronology, Lu-Hf isotopes and REE geochemistry constrains on the provenance and tectonic setting of Indochina Block in the Paleozoic. Tectonophysics, 677–678, 125–134.

Wang Y., Wang Y.K., Qian X., Zhang Y.Z., Gan C.S., Senebouttalath V., Wang Y., 2020. Early Paleozoic subduction in the Indochina interior: Revealed by Ordo-Silurian mafic-intermediate igneous rocks in South Laos. Lithos, 362–363, 105488.

Whitney D.L., Evans B.W., 2010. Abbreviations for names of rock-forming minerals. American Mineralogist, 95(1), 185–187.

Wu C.M., 2017. Calibration of the garnet-biotite-Al_2SiO_5-quartz geobarometer for metapelites. Journal of Metamorphic Geology, 35(9), 983–998.

Wu C.M., 2020. Calibration of the biotite-muscovite geobarometer for metapelitic assemblages devoid of garnet or plagioclase. Lithos, 372–373, 105668.

Wu C.M., Zhao G.C., 2006. Recalibration of the garnet-muscovite (GM) geothermometer and the garnet-muscovite-plagioclase-quartz (GMPQ) geobarometer for metapelitic assemblages. Journal of Petrology, 47, 2357–2368.

Wu C.M., Chen H.X., 2015. Revised Ti-in-biotite geothermometer for ilmenite-or rutile bearing crustal metapelites. Science Bulletin, 60, 116–121.